Title

Element-Specific Study of Magnetic Anisotropy and Hardening in SmCo5—x Cu x Thin Films

Journal

Inorganic Chemistry, 62(40)

ISSN

0020-1669

Authors

Gkouzia, Georgia

Günzing, Damian

Xie, Ruiwen

et al.

Publication Date

2023-10-09

DOI

10.1021/acs.inorgchem.3c01768

Inorganic Chemistry

pubs.acs.org/IC
Article

Element-Specific Study of Magnetic Anisotropy and Hardening in $SmCo_{5-x}Cu_x$ Thin Films

Georgia Gkouzia,* Damian Günzing, Ruiwen Xie,* Teresa Weßels, András Kovács, Alpha T. N'Diaye, Márton Major, J. P. Palakkal, Rafal E. Dunin-Borkowski, Heiko Wende, Hongbin Zhang, Katharina Ollefs, and Lambert Alff

Cite This: *Inorg. Chem.* 2023, 62, 16354−16361

ABSTRACT: This work investigates the effect of copper substitution on the magnetic properties of $SmCo_5$ thin films synthesized by molecular beam epitaxy. A series of thin films with varying concentrations of Cu were grown under otherwise identical conditions to disentangle structural and compositional effects on the magnetic behavior. The combined experimental and theoretical studies show that Cu substitution at the Co_{3g} sites not only stabilizes the formation of the $SmCo_5$ structure but also enhances magnetic anisotropy and coercivity. Density functional theory calculations indicate that $Sm(Co_4Cu_{3g})_5$ possesses a higher single-ion anisotropy as compared to pure $SmCo_5$. In addition, X-ray magnetic circular dichroism reveals that Cu substitution causes an increasing decoupling of the Sm 4f and Co 3d moments. Scanning transmission electron microscopy confirms predominantly $SmCo_5$ phase formation and reveals nanoscale inhomogeneities in the Cu and Co distribution. Our study based on thin film model systems and advanced characterization as well as modeling reveals novel aspects of the complex interplay of intrinsic and extrinsic contributions to magnetic hysteresis in rare-earth-based magnets, i.e., the combination of increased intrinsic anisotropy due to Cu substitution and the extrinsic effect of inhomogeneous elemental distribution of Cu and Co.

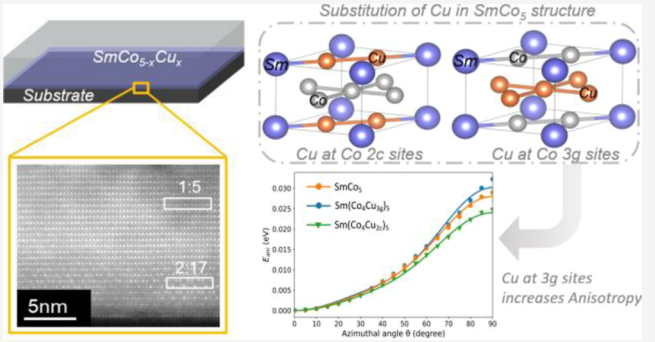

1. INTRODUCTION

$SmCo_5$-based permanent magnets were developed in the 1960s and were known to possess an extremely strong uniaxial magnetic anisotropy of about K_1 = 17.2 MJ/m^3.[1−3] The large magnetocrystalline anisotropy energy (MAE) arises due to the spin−orbit coupling of the localized and partially filled 4f shell of Sm and the spin−orbit coupling of the itinerant 3d electrons of cobalt in a strong crystal electric field.[4,5] Besides, $SmCo_5$ exhibits a relatively large energy product $(BH)_{max}$ up to 200 kJ/m^3 and a Curie temperature of 1020 K. The $SmCo_5$ phase has a hexagonal crystal structure with a space group of *P6/mmm*.

In practical applications, $SmCo_5$-based permanent magnets are widely used in motors, generators, actuators, etc.[6] These magnets are made from complex alloys, such as Sm−Co−Cu−Fe−Zr derived from the Sm_2Co_{17}-type, and require sophisticated heat treatments during fabrication, which lead to the emergence of a unique microstructure.[7,8] The increased demand for high $(BH)_{max}$ magnets, in particular for high-temperature applications in renewable energy technologies, has spurred recent interest in the various phenomena leading to high coercivity.[6,9] It is well-known that phase decomposition of the starting alloy results in a cellular microstructure of Sm_2Co_{17} (2:17) with a $SmCo_5$ (1:5) intergranular phase and a Zr-rich platelet.[10,11] The $SmCo_5$ phase is Cu-rich, and the Sm_2Co_{17} phase is Fe-rich. The magnetic properties of $SmCo_{5-x}Cu_x$ polycrystalline bulk at low temperatures were studied by Oesterreicher et al. in 1979. In this paper, the largest increase in coercivity was observed for Cu substitution levels of x = 4 in $SmCo_{5-x}Cu_x$.[12] Over the years, various studies have investigated the role of the individual elements Cu, Fe, and Zr in intrinsic and extrinsic magnetic properties.[13] Nevertheless, a complete understanding that could help overcome the so-called Brown's paradox and help in the development of novel green magnets is still lacking.[14−17]

Sm−Co thin films offer precise control over nanostructure, making them an ideal candidate for providing model structures

Received: June 1, 2023
Published: September 22, 2023

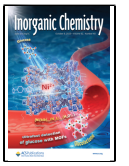

https://doi.org/10.1021/acs.inorgchem.3c01768
Inorg. Chem. 2023, 62, 16354−16361

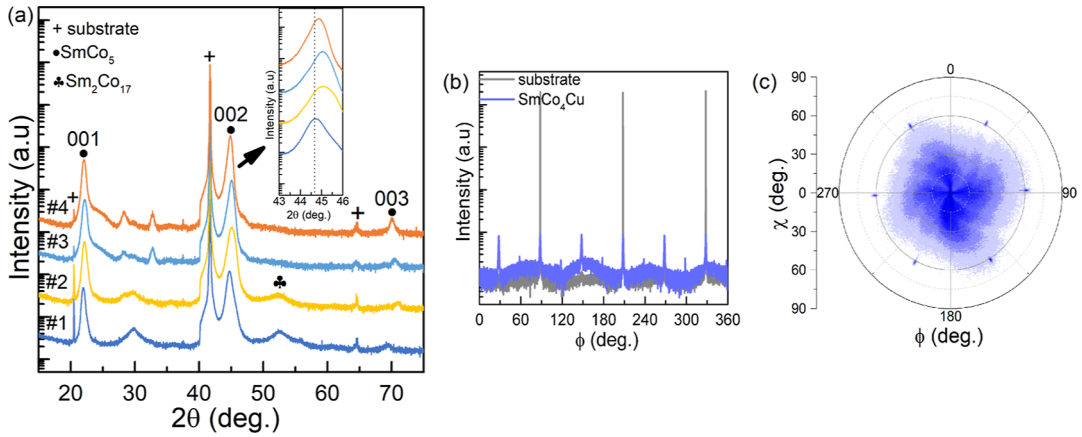

Figure 1. (a) θ–2θ XRD patterns of (#1) $SmCo_{4.5}Cu_{0.5}$, (#2) $SmCo_4Cu$, (#3) $SmCo_{3.5}Cu_{1.5}$, and (#4) $SmCo_3Cu_2$ thin films grown onto a single crystalline Al_2O_3 substrate at 550 °C. At 41.67°, the 006 reflection of the Al_2O_3 substrate is marked with the plus sign. (b) ϕ Scan of the $SmCo_4Cu$ film (blue) grown on a single crystalline Al_2O_3 substrate (gray) at 550 °C. (c) Pole figure of the $SmCo_5$ reflection of the $SmCo_4Cu$ film.

to understand the specific role of individual defects on the magnetic properties. Nevertheless, due to the thermodynamic instability of the $SmCo_5$ phase, in thin films, complex decomposition phenomena do occur. We have recently discovered a novel phase decomposition regime in molecular-beam epitaxy (MBE)-grown thin films, resulting in the coexistence of $SmCo_5$ and Sm_2Co_{17} blocks at the nanoscale with a width of only a few nanometers.[18] These films have low coercivity due to their high crystallinity, phase purity, and fully coherent interfaces between $SmCo_5$ and Sm_2Co_{17}. In contrast, sputtered thin films grown at much higher particle energies have a more complex precipitation nanostructure made up of various Sm-rich phases such as $SmCo_3$ and Sm_2Co_7, which can lead to ultra-high coercivity primarily due to pinning at low-symmetry grain boundaries.[19]

Typically, different buffers and underlayers made from Ru, Cr, or Cu have been used to ease the growth of Sm–Co thin films. Textured Cr and Ru buffer layers promote the *c*-axis orientation and improve the magnetic properties. Above all, Cu has been widely studied because it not only facilitates the out-of-plane orientation but also has been found to have the unique advantage of stabilizing the $CaCu_5$ structure.[20−22] Nevertheless, the magnetic properties of the Sm–Co layer will be affected by diffusion processes from these buffer layers.

In this work, we have established a direct growth process of Cu-substituted $SmCo_{5-x}Cu_x$ samples on sapphire without using any additional underlayer, which eliminates the potential impact of diffusing elements. We use computational and experimental methods to characterize the element-specific magnetic properties and illuminate the role of Cu incorporation in $SmCo_5$ and its effect on coercivity.

2. METHODOLOGY

2.1. Experimental Part. The base pressure of the used MBE chamber was 10^{-10} mbar. The $SmCo_{5-x}Cu_x$ thin films were deposited by e-beam co-evaporation from elemental Sm, Co, and Cu sources. The films were deposited onto *c*-axis-oriented Al_2O_3 substrates, known to promote the *c*-axis orientation of the $SmCo_5$ phase. First, a temperature scan was carried out showing that the most favorable temperature for growing a crystalline $SmCo_5$ layer in this setup was 550 °C. The substrates were heated from the backside using a diode laser, a technique that avoids contamination from vacuum heaters. Before evaporation, the substrates were annealed at 540 °C for 1 h in the MBE chamber to obtain a clean crystalline substrate surface. For all samples, the deposition rate of the samarium was kept constant at 0.1 Å/s. The individual deposition rates of cobalt and copper were changed, but the sum of the deposition rate (Co plus Cu) was kept constant at 0.1 Å/s. A series of $SmCo_{5-x}Cu_x$ films were produced with x = 0.5, 1, 1.5, and 2. The evaporation rates during the growth of the thin films were controlled by using quartz crystal microbalances. The quality of the films was monitored using in situ reflection high-energy electron diffraction.

X-ray diffraction (XRD) with Cu Kα radiation on a Rigaku SmartLab system was carried out for the crystallographic and structural characterization of the films. The thicknesses of the films were determined to be 30 nm ± 2 nm. The magnetic properties of the films were measured by a superconducting quantum interference device (SQUID) in two directions, out-of-plane (OOP) and in-plane (IP) of the substrate surface, using the MPMS-XL magnetometer by Quantum design. The measurements have been performed at 300 K with external fields up to 6 tesla. The diamagnetic contribution from the Al_2O_3 substrate has been subtracted by correcting the slope between 4 and 6 tesla. The coupling of Sm and Co moments has been studied using X-ray magnetic circular dichroism (XMCD) by recording element-specific hysteresis loops. For structural and spectroscopic characterizations, scanning transmission electron microscopy (STEM) and energy-dispersive X-ray spectroscopy (EDX)[23] were used in combination on cross-sectional specimens that were prepared along the *c*-axis using a focused Ga ion beam (FIB) sputtering. The STEM images and EDX maps were processed using Velox software (Thermo Fisher Scientific).

2.2. Computational Part. In order to evaluate the single-ion anisotropy (SIA) of Sm^{3+}, the crystal field parameters (CFPs) were calculated in the framework of density functional theory (DFT) using the WIEN2k program.[24] The generalized gradient approximation was employed for the exchange–correlation functional. The experimental lattice parameters of $SmCo_5$ were adopted in the calculations. Regarding the Cu-doped cases, including $Sm(Co_4Cu_{3g})_5$ and $Sm(Co_4Cu_{2c})_5$, the lattice parameters were fixed to those of $SmCo_5$ considering the relatively small volume change. Therefore, the solely chemical effect of Cu can be explicitly probed. The RMT ×

https://doi.org/10.1021/acs.inorgchem.3c01768
Inorg. Chem. 2023, 62, 16354−16361

K_{max} was set to 7, and a k-mesh of 9 × 9 × 9 was sampled in the Brillouin zone. For the calculation of CFPs, we followed the method proposed by Novák et al.,[25] in which the local Hamiltonian in the basis of Wannier functions is expanded by a series of spherical tensor operators. In specific, the self-consistent field (SCF) calculation was first performed without spin polarization and with 4f electrons in the core. Subsequently, a non-SCF calculation was carried out treating 4f as valence states so that the 4f states were allowed to hybridize with the transition metal 3d states. In addition, we shifted the energy of 3d states 0.4 Ry lower to assure appropriate hybridization strength. The Bloch states from the 4f energy window were then transformed to Wannier functions using the Wien2wannier interface[26] followed by the standard Wannierization process by Wannier90.[27]

The obtained CFPs were then used to construct the atomic Hamiltonian of Sm by including the Coulomb interactions ($\hat{H}_U$), the spin−orbit coupling, and the Sm-transition metal exchange coupling ($\hat{H}_{ex}$)

$$\hat{H}_{at} = \hat{H}_U + \lambda \sum_i \hat{s}_i \hat{l}_i + \hat{H}_{CF} + \hat{H}_{ex} \quad (1)$$

The eigenvalue of the Hamiltonian was solved using the Lanczos algorithm as implemented in the Quanty code.[28] By varying the magnetization direction corresponding to the exchange coupling term, the eigenvalue was then obtained as a function of azimuthal angle, which give rise to the SIA.

3. RESULTS AND DISCUSSION

3.1. Crystal Structure. Figure 1a shows the XRD patterns of the $SmCo_{5-x}Cu_x$ films grown onto 001-oriented Al_2O_3 substrates. The main 006 reflection of the substrate appears at 41.67°. The 001-oriented Al_2O_3 promotes the growth of c-axis-textured $Sm(Co,Cu)_5$ films, as indicated by the presence of 00l-type reflections.

In the XRD patterns, we observe reflections assigned to the $SmCo_5$ and Sm_2Co_{17} phases. In Table 1, the lattice parameters c of our thin films are listed, and the bulk $SmCo_5$ and Sm_2Co_{17} values are given as references 29, 30. Our c-axis values for $SmCo_{5-x}Cu_x$ with x = 1.5 and x = 2 are close to literature values, while our values for x = 0.5 and x = 1 are larger. This observed non-linear peak shift of the 002 reflection shown in the inset of Figure 1a can be consistently explained when considering that at this position the 002 reflection from the 1:5 and the 004 reflection from the 2:17 phase overlap, with the 004 reflection of 2:17 at a lower diffraction angle as observed previously.[18] Therefore, when the 2:17 phase is eliminated at increased Cu content ($x \approx 1.5$), the peak maximum shifts close to the expected value of $SmCo_{3.5}Cu_{1.5}$. For $x \geq 1.5$, the values coincide again with the expected bulk values. Note that the phase purity of the 1:5 phase is significantly higher than that of typical sputtered thin films; however, reflections from a small amount of residual Sm-rich phases can still be detected around 29 and 30°. Nevertheless, the overall crystal structure remains consistent predominantly 1:5 throughout the series.

Table 1. Lattice Parameters c and 2θ Values for the Series of the $SmCo_{5-x}Cu_x$ Thin Films[a]

sample name	c lattice parameter (Å)	2θ (deg)
$SmCo_{4.5}Cu_{0.5}$	4.0505	44.711
$SmCo_4Cu$	4.015	45.116
$SmCo_{3.5}Cu_{1.5}$ (bulk)	4.01	45.186
$SmCo_{3.5}Cu_{1.5}$	4.022	45.043
$SmCo_3Cu_2$	4.037	44.861
$SmCo_5$ (bulk)	4.006	45.233
Sm_2Co_{17} (bulk)	12.233	44.393

[a]The bulk values are taken from ref 30 for reference.

Azimuth scans have been used to confirm crystal lattice symmetry and epitaxial relations. Here, we show a ϕ-scan of the diffraction peak of the $SmCo_4Cu$ sample with respect to the substrate. Figure 1b shows the 104 reflection (gray 2θ = 35.03° and χ = 38.02°) of the substrate which is rhombohedral and the $SmCo_4Cu$ sample (blue) which is hexagonal. The ϕ-scan shows three peaks which indicate the 3-fold symmetry of the Al_2O_3 substrate. Six peaks are obtained for the $SmCo_4Cu$ film which shows the 6-fold symmetry and proves its hexagonal phase. The observed peaks correspond to the 201 reflection of the $SmCo_5$ phase. The pole figure of the 201 reflections, Figure 1c, shows the high-intensity Bragg peaks in blue. The distribution of the reflections indicates a crystalline, highly textured film.

3.2. Magnetization Measurements. Cu is usually used as a dopant in $SmCo_5$ thin films grown onto Cr or Ru buffer layers.[31,32] As mentioned above, in this work, no additional underlayers have been used, and the $SmCo_{5-x}Cu_x$ films were deposited directly on top of Al_2O_3 substrates. The hysteresis loops of the out-of-plane direction are shown in Figure 2. The easy axis of magnetization is out-of-plane for all samples, while the hard axis is in-plane, as shown in Figure 3. Starting from the film with the lowest Cu concentration, a remanent magnetization of 0.6 T can be observed and the coercivity reaches 1.08 T. Upon increasing the Cu ratio, the coercivity drastically increases up to 1.64 T, whereas the remanent and saturation magnetizations, as expected due to Cu dilution of Co moments, decrease (see Figure 4). A further increase of Cu results in a rapid decrease of coercivity to 1.23 T.

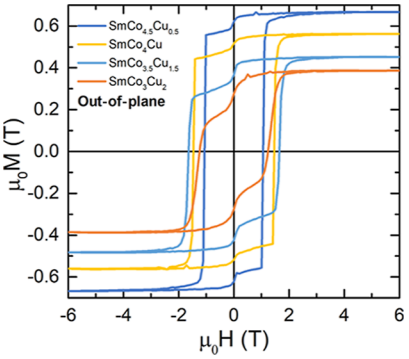

Figure 2. Magnetization curves of the $SmCo_{5-x}Cu_x$ thin films measured in the OOP direction as a function of the applied field at 300 K.

There are two sites where Cu can substitute Co, namely, Co_{2c} and Co_{3g}, as shown in Figure 5.[33] As the thin film microstructure is similar in all cases predominantly 1:5, we assume that extrinsic contributions to the coercivity are comparable—but with the exception of the distribution of the substitutional element copper. The Cu distribution will be addressed in Section 3.4. Therefore, we suggest that the increased coercivity is at least partly correlated with an increased intrinsic anisotropy resulting from Cu substitution at

https://doi.org/10.1021/acs.inorgchem.3c01768
Inorg. Chem. 2023, 62, 16354−16361

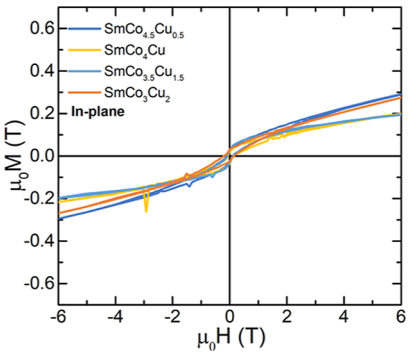

Figure 3. Magnetization curves of the $SmCo_{5-x}Cu_x$ thin films measured in the IP direction as a function of the applied field at 300 K.

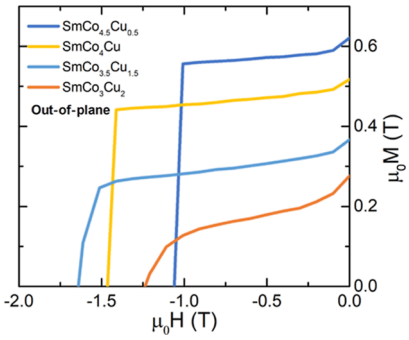

Figure 4. Demagnetization curves of the $SmCo_{5-x}Cu_x$ thin films as a function of the applied field at 300 K.

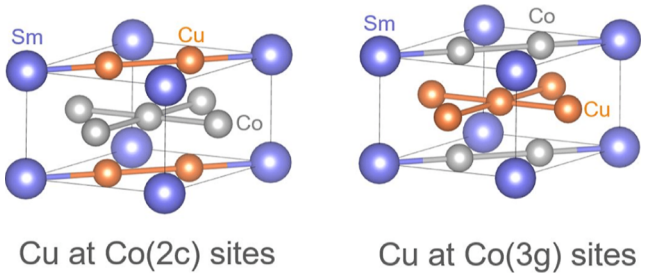

Figure 5. Schematic representation of the occupation of Cu at Co 2c sites and at Co 3g sites in the $SmCo_5$ crystal structure.

the Co_{3g} sites. A similar suggestion has been made for $Y(Co,Cu)_5$,[34] a system which also behaves in thin films similar to the here investigated $Sm(Co,Cu)_5$.[18,35] To corroborate this hypothesis, we discuss the described DFT-based modeling in Section 3.5. The IP magnetization measurements shown in Figure 3 further support an increased anisotropy for $SmCo_4Cu$ and $SmCo_{3.5}Cu_{1.5}$. Another factor leading to increased intrinsic anisotropy is the improved crystallization of the 1:5 phase due to Cu substitution.[36] Interestingly, in the OOP loops shown in Figure 4, a small kink appears at the zero field. This kink might be associated with the presence of a residual soft magnetic nanocrystalline or amorphous phase that is not strongly coupled to the hard-magnetic phase.[37]

3.3. Element-Specific Measurements. XMCD spectra and element-specific hysteresis curves have been recorded at the bending magnet beamline 6.3.1 of the Advanced Light Source (ALS) at the Lawrence Berkeley National Laboratory. The measurements were carried out using an applied magnetic field of up to 1.9 T with a fixed polarization at ambient temperatures. The samples have been measured in the OOP direction, parallel to the magnetic easy *c*-axis. As a detection method, X-ray-excited optical luminescence (XEOL) was used, which probes the full thickness of the film, due to the luminescence of oxygen in the Al_2O_3 substrate.[38] In this way, element-specific hysteresis loops have been recorded at fixed energies at the XMCD maxima and minima for Co $L_{2,3}$-edges (779.2 and 794.5 eV) and Sm $M_{4,5}$-edges (1082.5 and 1109.3 eV).

The strength of element-specific hysteresis measurements is the quantitative separation of the individual contributions from the Co and Sm magnetic moments.[39] The normalized element-specific hysteresis curves are shown in Figure 6. The Co and

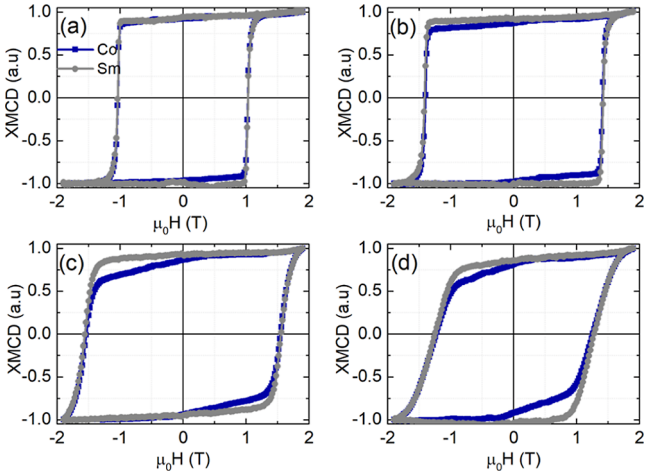

Figure 6. Element-specific hysteresis loops for the Sm $M_{4,5}$ (gray) and Co $L_{2,3}$-edges (blue) recorded at room temperature applying positive and negative 1.9 T external fields in the OOP direction for the following samples (a) $SmCo_{4.5}Cu_{0.5}$, (b) $SmCo_4Cu$, (c) $SmCo_{3.5}Cu_{1.5}$, and (d) $SmCo_3Cu_2$.

Sm curves do not deviate significantly for the $SmCo_{4.5}Cu_{0.5}$ film shown in Figure 6a. This confirms the stronger exchange coupling between the rare-earth Sm and the transition metal Co. Upon the increase of Cu substitution, a gap between Co and Sm appears in the second quadrant's demagnetizing curves. The measured data indicates that the substitution of Cu in the Co sub-lattice causes a continuous decoupling of the Sm and Co moments and softens the Co moment. The dilution with Cu is also the reason for the reduced total magnetization of the films. In contrast, samarium moments are only softened at higher Cu concentrations, which is also supported by the reduced critical temperature of the Cu-rich compounds.

3.4. Structure and Chemical Composition of $SmCo_4Cu$. The structure and elemental distribution of the $SmCo_4Cu$ sample were studied in cross-sectional geometry. Figure 7a shows the structure of the sample in a high-resolution high-angle annular dark-field (HAADF) STEM image. Note the presence of a characteristic "dumbbell" pattern in the Sm-Co-Cu that indicates the formation of the 2:17 phase at the interface to the Al_2O_3 substrate. The rest of the layer shows a uniform 1:5 phase formation. The thickness of the 2:17 phase is approximately 7 nm. The transition from 2:17 to 1:5 phase is continuous, i.e., no sharp boundaries were observed.

Figure 7b shows the chemical composition distribution of individual elements extracted from EDX/STEM spectrum

https://doi.org/10.1021/acs.inorgchem.3c01768
Inorg. Chem. 2023, 62, 16354−16361

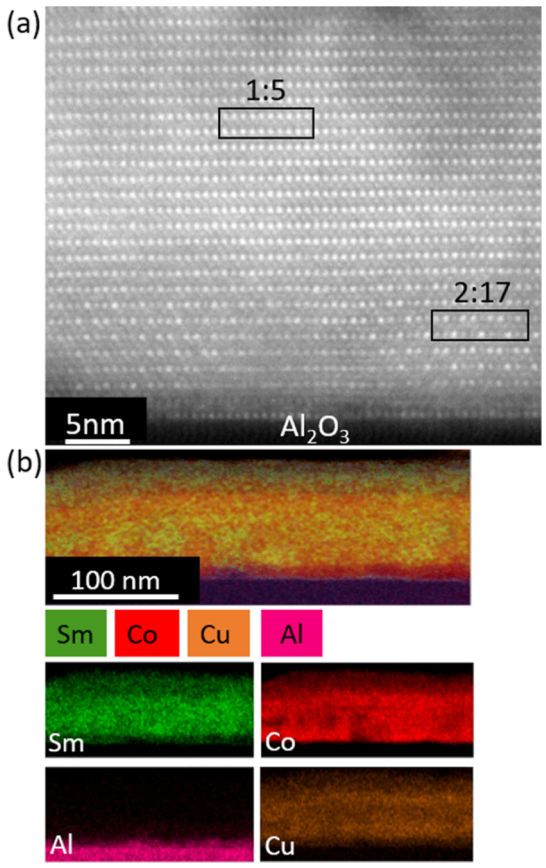

Figure 7. (a) High-resolution HAADF STEM image showing the interface of the $SmCo_4Cu$ thin film to the Al_2O_3 substrate. The dumbbell pattern of atomic columns reveals the presence of the Sm_2Co_{17} phase. (b) Chemical composition mapping of Sm, Co, and Cu extracted from STEM/EDX spectrum imaging. Note that the distribution of Co and Cu is not uniform.

imaging. The Co and Cu maps reveal an inhomogeneous distribution of the elements, suggesting Cu- and Co-rich regions. These inhomogeneities might be responsible for the zero-field kink in the SQUID measurement, which is absent in the XMCD measurement (see Figures 4 and 6).

3.5. Discussion. The magnetization curves of the $SmCo_{5-x}Cu_x$ films measured at room temperature are shown in Figure 2. It is clear that Cu substitution affects the coercivity which reaches a maximum value of 1.64 T. The presence of Cu at low concentrations enhances coercivity up to the $SmCo_{3.5}Cu_{1.5}$. Following the XRD patterns, the 1:5 phase is by far the predominant phase in all samples. A small fraction of the 2:17 phase which seems to be induced from the substrate (rather than to a nanoscale phase decomposition as described previously)[18] is fully suppressed for higher Cu substitution. XMCD element-specific hysteresis loops proved that Cu substitution results in an increasing decoupling of the Sm and Co moments. Last but not least, electron microscopy measurements showed that the films are dominated mainly by the 1:5 phase.

We first discuss the effect of Cu substitution on the intrinsic magnetic anisotropy of $SmCo_5$, especially the SIA of Sm^{3+}. While intuitively one would expect an immediate decrease of intrinsic magnetic anisotropy, the computational methods described in Section 2.2 show a different and more complex behavior. The calculated CFPs B_{lm} for $SmCo_5$, $Sm(Co_4Cu_{3g})_5$, and $Sm(Co_4Cu_{2c})_5$ are listed in Table 2. $SmCo_5$ belongs to the point group D_{6h}; therefore, only B_{20}, B_{40}, B_{60}, and $B_{6\pm6}$ retain. In particular, the magnitude of B_{20} is dominant and determines largely the magnetic anisotropy of Sm^{3+}, i.e., a negative B_{20} indicates uniaxial magnetic anisotropy. Note that the energy shift for transition metal 3d states was selected to be −0.4 Ry. By varying the energy shift to −0.2 and −0.6 Ry, the corresponding B_{20} are −1328 and −977 K, respectively. In addition, depending on the specific experimental measurement and fitting methods, the values of CFPs, especially for B_{40}, B_{60}, and $B_{6\pm6}$, could differ largely. The value of B_{20} with an energy shift of −0.4 Ry in the current work is comparable with those of refs 40 and 41. Here, we would like to stress that we control the value of the energy shift to be the same for $SmCo_5$ and Cu-doped $SmCo_5$, so that the CFP difference can be ascribed to the potential difference Sm senses in the different crystalline environments. With Cu occupying the 3*g* sites (Figure 5), B_{20} is more negative, indicating that the SIA of Sm^{3+} is indeed enhanced. In contrast, the Cu doping on the 2*c* site tends to lower the SIA of Sm^{3+}. Note that the number of nonzero B_{lm} parameters in $Sm(Co_4Cu_{3g})_5$ is larger due to the lower symmetry.

Another important aspect to be considered is the exchange coupling between the Sm and its neighboring Co atoms, which can be weakened upon introducing non-magnetic Cu atoms into the system. The exchange field in $SmCo_5$ is set to be 250 T according to previous experimental[42] and theoretical[41] work, while for $Sm(Co_4Cu_{3g})_5$ and $Sm(Co_4Cu_{2c})_5$, the exchange fields are rescaled based on the calculated J_{SmCo} values contributed from the first-nearest neighbors of Sm with respect to the J_{SmCo} of $SmCo_5$. Such exchange coupling parameters are evaluated using the OpenMX[46] code in the LDA + *U* regime, with *U* = 6.7 eV and *J* = 0.7 eV for the Sm 4f states. Accordingly, we set the exchange fields of Sm-

Table 2. CFPs (in Units of Kelvin) for $Sm^{3+}Co_5$, $Sm^{3+}(Co_4Cu_{3g})_5$, and $Sm^{3+}(Co_4Cu_{2c})_5$[a]

B_{lm} (K)	$SmCo_5$	Sankar ref 40	Tils ref 42	Tie-Song ref 43	Givord ref 44	Buschow ref 45	Patrick ref 41	$Sm(Co_4Cu_{3g})_5$	$Sm(Co_4Cu_{2c})_5$
B_{20}	−1068	−840	−652	−660	−400	−360	−800	−1380	−867
$B_{2\pm2}$								168	
B_{40}	5	200		−360	0	0	−177	77	−91
$B_{4\pm2}$								102	
$B_{4\pm4}$								−44	
B_{60}	−473	0		0	800	0	71	−472	−430
$B_{6\pm2}$								−14	
$B_{6\pm4}$								−34	
$B_{6\pm6}$	494	6		0	0	0	−121	501	456

[a]For comparison, the experimental values and one theoretical result (ref 41) are also listed.

https://doi.org/10.1021/acs.inorgchem.3c01768
Inorg. Chem. 2023, 62, 16354−16361

$(Co_4Cu_{3g})_5$ and $Sm(Co_4Cu_{2c})_5$ to 201 and 230 T, respectively. The Coulomb interaction parameters and the spin−orbit coupling strength are taken from ref 47. By varying the exchange field direction which is represented by the azimuthal angle θ, Figure 8 shows the eigenvalue Eani of $\hat{H}_{at}$ as a function

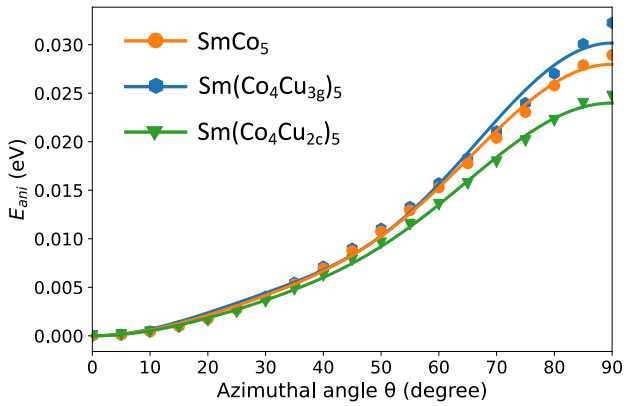

Figure 8. Ground-state energy of the Sm 4f shell in $SmCo_5$ (orange circle), $Sm(Co_4Cu_{3g})_5$ (blue hexagons), and $Sm(Co_4Cu_{2c})_5$ (green triangle) as a function of magnetization direction represented by the azimuthal angle θ.

of θ. It can be explicitly observed that Sm^{3+} in $Sm(Co_4Cu_{3g})_5$ possesses the highest SIA, while in $Sm(Co_4Cu_{2c})_5$, the SIA is the lowest. By fitting the energy curve to

$$E_{ani}(\theta) = K_1 \sin^2\theta + K_2 \sin^4\theta + K_3 \sin^6\theta \quad (2)$$

we obtain K_1 of 21, 24, and 17 meV for $SmCo_5$, $Sm(Co_4Cu_{3g})_5$, and $Sm(Co_4Cu_{2c})_5$, respectively. Note here that we omit the K_3' term associated with $K_3' \sin^6\theta \cos 6\phi$ since we find K_3' rather small. Besides, the Cu doping effect on the Co sites can be approximated using YCo_5 as a prototype. It has been reported that the 3*g*-site doping of Cu increases the magnetic anisotropy of YCo_5,[34] while the 2*c*-site doping is expected to reduce the magnetic anisotropy due to a larger K_1 of Co_{2c} than that of Co_{3g}. In addition, according to our DFT calculations, the 2*c*-site doping is slightly energetically favorable by about 7 meV/atom as compared to the 3*g*-site doping. This strongly implies a statistically random distribution on both sites in reality as 7 meV amounts to a temperature of 81 K. Therefore, considering the contrasting roles played by Cu with different Wyckoff position occupations, a non-monotonous change of magnetic anisotropy with Cu doping content can be expected, as also observed in the Ce−Co-based systems.[48,49] It is intriguing to characterize the intrinsic properties of the Cu-substituted $SmCo_5$ system to bridge the gap between the microscopic equilibrium properties and the macroscopic coercivity.[50]

From a macroscopic point of view, Sm-rich precipitates as well as the formation of many different Sm−Co phases and structural disorder phenomena are strongly connected to high coercivity values in sputtered Sm−Co films.[19] Sayama et al.[51] suggested that the origin of high perpendicular anisotropy in $SmCo_5$ thin films on Cu buffer layers is related to the diffusion of Cu atoms into the $SmCo_5$ structure. Note that this diffusion effect is excluded in the presented study. The layer of Sm_2Co_{17} at the substrate interface will not contribute to a systematic change of the hysteresis itself. As the defect structure is similar throughout the consistent series of thin films, we correlate the increased coercivity to the increased intrinsic magnetocrystalline anisotropy upon Cu substitution and to the inhomogeneous distribution of Cu and Co. Since other phases, grain boundaries, and phase boundaries can be excluded for our thin film model systems, we suggest the nanoscale disproportionation of Cu and Co as an additional novel source of coercivity leading to enhanced pinning with increased Cu substitution.

4. CONCLUSIONS

In summary, our investigation of highly crystalline $SmCo_{5-x}Cu_x$ thin films grown by MBE on Al_2O_3 substrates in combination with advanced computational and characterization methods has revealed that copper substitution enhances the intrinsic magnetic anisotropy, correlated with an increase in coercivity. As a second source of increased coercivity, we have identified with EDX measurements a disproportionation of Cu- and Co-rich areas within an otherwise homogeneous 1:5 phase structure. The practical applicability of Cu to replace Co is limited of course by the induced overall reduction of the total magnetic moment, acting negatively on the $(BH)_{max}$ product. XMCD provided clear evidence of a decoupling of Sm and Co moments in the presence of Cu. Electron microscopy confirmed the presence of the small amount of interfacial Sm_2Co_{17} phase in the highly crystalline $SmCo_5$ layer. Based on thin film model systems, our study provides novel insight into the complex materials science and hardening mechanisms in rare-earth-based permanent magnetic materials by disentangling different sources of intrinsic and extrinsic contributions to the hysteresis behavior.

AUTHOR INFORMATION

Corresponding Authors

Georgia Gkouzia − *Institute of Materials Science, Technical University of Darmstadt, 64287 Darmstadt, Germany;* orcid.org/0009-0002-7527-6637; Email: georgia.gkouzia@tu-darmstadt.de

Ruiwen Xie − *Institute of Materials Science, Technical University of Darmstadt, 64287 Darmstadt, Germany;* Email: ruiwen.xie@tmm.tu-darmstadt.de

Authors

Damian Günzing − *Faculty of Physics and Center for Nanointegration (CENIDE), University of Duisburg-Essen, 47057 Duisburg, Germany; Lawrence Berkeley National Laboratory, Berkeley, California 94720, United States*

Teresa Weßels − *Ernst Ruska-Centre for Microscopy and Spectroscopy with Electrons and Peter Grünberg Institute, Forschungszentrum Jülich, 52428 Jülich, Germany; Faculty of Physics and Center for Nanointegration (CENIDE), University of Duisburg-Essen, 47057 Duisburg, Germany*

András Kovács − *Ernst Ruska-Centre for Microscopy and Spectroscopy with Electrons and Peter Grünberg Institute, Forschungszentrum Jülich, 52428 Jülich, Germany;* orcid.org/0000-0001-8485-991X

Alpha T. N'Diaye − *Lawrence Berkeley National Laboratory, Berkeley, California 94720, United States*

Márton Major − *Institute of Materials Science, Technical University of Darmstadt, 64287 Darmstadt, Germany*

J. P. Palakkal − *Institute of Materials Physics, Georg-August-University of Göttingen, 37077 Göttingen, Germany; Institute of Materials Science, Technical University of Darmstadt, 64287 Darmstadt, Germany;* orcid.org/0000-0002-7183-2627

https://doi.org/10.1021/acs.inorgchem.3c01768
Inorg. Chem. 2023, 62, 16354−16361

Rafal E. Dunin-Borkowski − *Ernst Ruska-Centre for Microscopy and Spectroscopy with Electrons and Peter Grünberg Institute, Forschungszentrum Jülich, 52428 Jülich, Germany;* orcid.org/0000-0001-8082-0647
Heiko Wende − *Faculty of Physics and Center for Nanointegration (CENIDE), University of Duisburg-Essen, 47057 Duisburg, Germany;* orcid.org/0000-0001-8395-3541
Hongbin Zhang − *Institute of Materials Science, Technical University of Darmstadt, 64287 Darmstadt, Germany*
Katharina Ollefs − *Faculty of Physics and Center for Nanointegration (CENIDE), University of Duisburg-Essen, 47057 Duisburg, Germany*
Lambert Alff − *Institute of Materials Science, Technical University of Darmstadt, 64287 Darmstadt, Germany;* orcid.org/0000-0001-8185-4275

Complete contact information is available at: https://pubs.acs.org/10.1021/acs.inorgchem.3c01768

Notes

The authors declare no competing financial interest.

■ ACKNOWLEDGMENTS

We acknowledge the financial support from the Deutsche Forschungsgemeinschaft (DFG) in the framework of the CRC/TRR 270 (Project ID. 405553726), projects A02, A03, A05, B05, and Z01/02. J.P.P. acknowledges the German Research Foundation (Deutsche Forschungsgemeinschaft - DFG) for the funding under project 429646908. The authors acknowledge Janghyun Jo for experimental help and Lea Risters for FIB sample preparation. This research used the resources of the Advanced Light Source, which is a DOE Office of Science User Facility under contract no. DE-AC02-05CH11231.

■ REFERENCES

(1) Coey, J. M. *Magnetism and Magnetic Materials*; Cambridge University Press: Cambridge, U.K., 2010.
(2) Strnat, K.; Hoffer, G.; Olson, J.; Ostertag, W.; Becker, J. A family of new cobalt-base permanent magnet materials. *J. Appl. Phys.* **1967**, *38*, 1001−1002.
(3) Strnat, K. Rare earth-cobalt permanent magnets. *Handb. Ferromagn. Mater.* **1988**, *4*, 131−209.
(4) Larson, P.; Mazin, I. Magnetic properties of $SmCo_5$ and YCo_5. *J. Appl. Phys.* **2003**, *93*, 6888−6890.
(5) Ucar, H.; Choudhary, R.; Paudyal, D. An overview of the first principles studies of doped RE-TM_5 systems for the development of hard magnetic properties. *J. Magn. Magn. Mater.* **2020**, *496*, 165902.
(6) Gutfleisch, O.; Willard, M. A.; Brück, E.; Chen, C. H.; Sankar, S.; Liu, J. P. Magnetic materials and devices for the 21st century: stronger, lighter, and more energy efficient. *Adv. Mater.* **2011**, *23*, 821−842.
(7) Mishra, R. K.; Thomas, G.; Yoneyama, T.; Fukuno, A.; Ojima, T. Microstructure and properties of step aged rare earth alloy magnets. *J. Appl. Phys.* **1981**, *52*, 2517−2519.
(8) Sepehri-Amin, H.; Thielsch, J.; Fischbacher, J.; Ohkubo, T.; Schrefl, T.; Gutfleisch, O.; Hono, K. Correlation of microchemistry of cell boundary phase and interface structure to the coercivity of Sm$(Co_{0.784}Fe_{0.100}Cu_{0.088}Zr_{0.028})_{7.19}$ sintered magnets. *Acta Mater.* **2017**, *126*, 1−10.
(9) Gutfleisch, O. High-temperature samarium cobalt permanent magnets. *Nanoscale Magnetic Materials and Applications*; Springer New York, 2009; pp 337−372. DOI: 10.1007/978-0-387-85600-1_12.
(10) Maury, C.; Rabenberg, L.; Allibert, C. Genesis of the cell microstructure in the Sm (Co, Fe, Cu, Zr) permanent magnets with 2:17 type. *Phys. Status Solidi* **1993**, *140*, 57−72.
(11) Duerrschnabel, M.; Yi, M.; Uestuener, K.; Liesegang, M.; Katter, M.; Kleebe, H.-J.; Xu, B.; Gutfleisch, O.; Molina-Luna, L. Atomic structure and domain wall pinning in samarium-cobalt-based permanent magnets. *Nat. Commun.* **2017**, *8*, 54.
(12) Oesterreicher, H.; Parker, F.; Misroch, M. Giant intrinsic magnetic hardness in $SmCo_{5-x}Cu_x$. *J. Appl. Phys.* **1979**, *50*, 4273−4278.
(13) Staab, F.; Bruder, E.; Schäfer, L.; Skokov, K.; Koch, D.; Zingsem, B.; Adabifiroozjaei, E.; Molina-Luna, L.; Gutfleisch, O.; Durst, K. Hard magnetic $SmCo_5$-Cu nanocomposites produced by severe plastic deformation. *Acta Mater.* **2023**, *246*, 118709.
(14) Hadjipanayis, G.; Tang, W.; Zhang, Y.; Chui, S.; Liu, J.; Chen, C.; Kronmuller, H. High temperature 2: 17 magnets: relationship of magnetic properties to microstructure and processing. *IEEE Trans. Magn.* **2000**, *36*, 3382−3387.
(15) Xiong, X. Y.; Ohkubo, T.; Koyama, T.; Ohashi, K.; Tawara, Y.; Hono, K. The microstructure of sintered Sm-$(Co_{0.72}Fe_{0.20}Cu_{0.055}Zr0.025)_{7.5}$ permanent magnet studied by atom probe. *Acta Mater.* **2004**, *52*, 737−748.
(16) Wu, S.; Zhang, D.-T.; Yue, M.; Wang, Y.-Q.; Shang, Z.-F.; Wu, D.; Liang, J.-M. In-situ observation of magnetization reversal process of $Sm(Co, Cu, Fe, Zr)_z$ magnets with different Fe contents. *Rare Met.* **2020**, *39*, 250−255.
(17) Shang, Z.; Yue, M.; Li, Y.; Zhang, D.; Xie, Z.; Wang, Y. The effect of multi-scale Cu distribution regulation on magnetic properties of $Sm(CoFeCuZr)_z$ magnets. *J. Magn. Magn. Mater.* **2020**, *502*, 166484.
(18) Sharma, S.; Zintler, A.; Günzing, D.; Lill, J.; Meira, D. M.; Eilhardt, R.; Singh, H. K.; Xie, R.; Gkouzia, G.; Major, M.; Radulov, I.; Komissinskiy, P.; Zhang, H.; Skokov, K.; Wende, H.; Takahashi, Y. K.; Ollefs, K.; Molina-Luna, L.; Alff, L. Epitaxy Induced Highly Ordered Sm_2Co_{17}−$SmCo_5$ Nanoscale Thin-Film Magnets. *ACS Appl. Mater. Interfaces* **2021**, *13*, 32415−32423.
(19) Akdogan, O.; Sepehri-Amin, H.; Dempsey, N.; Ohkubo, T.; Hono, K.; Gutfleisch, O.; Schrefl, T.; Givord, D. Preparation, characterization, and modeling of ultrahigh coercivity Sm−Co thin films. *Adv. Electron. Mater.* **2015**, *1*, 1500009.
(20) Seifert, M.; Neu, V.; Schultz, L. Epitaxial $SmCo_5$ thin films with perpendicular anisotropy. *Appl. Phys. Lett.* **2009**, *94*, 022501.
(21) Hofer, F. Physical metallurgy and magnetic measurements of $SmCo_5$-$SmCu_5$ alloys. *IEEE Trans. Magn.* **1970**, *6*, 221−224.
(22) Zhang, W.-y.; Zhang, X.-d.; Yang, Y.-c.; Shen, B.-g. Effect of Cu substitution on structure and magnetic properties of anisotropic SmCo ribbons. *J. Alloys Compd.* **2003**, *353*, 274−277.
(23) Ernst Ruska-Centre for Microscopy and Spectroscopy with Electrons. FEI Titan G2 80-200 CREWLEY. *J. Large Scale Res. Facil.* **2016**, *2*, A43.
(24) Blaha, P.; Schwarz, K.; Tran, F.; Laskowski, R.; Madsen, G. K.; Marks, L. D. WIEN2k An APW+ lo program for calculating the properties of solids. *J. Chem. Phys.* **2020**, *152*, 074101.
(25) Novák, P.; Knížek, K.; Kuneš, J. Crystal field parameters with Wannier functions: Application to rare-earth aluminates. *Phys. Rev. B* **2013**, *87*, 205139.
(26) Kuneš, J.; Arita, R.; Wissgott, P.; Toschi, A.; Ikeda, H.; Held, K. Wien2wannier: From linearized augmented plane waves to maximally localized Wannier functions. *Comput. Phys. Commun.* **2010**, *181*, 1888−1895.
(27) Mostofi, A. A.; Yates, J. R.; Lee, Y.-S.; Souza, I.; Vanderbilt, D.; Marzari, N. wannier90: A tool for obtaining maximally-localised Wannier functions. *Comput. Phys. Commun.* **2008**, *178*, 685−699.
(28) Lu, Y.; Höppner, M.; Gunnarsson, O.; Haverkort, M. Efficient real-frequency solver for dynamical mean-field theory. *Phys. Rev. B* **2014**, *90*, 085102.
(29) Song, X.; Lu, N.; Xu, W.; Zhang, Z.; Zhang, J. Phase transformation in nanocrystalline Sm_2Co_{17} permanent magnet material. *J. Appl. Crystallogr.* **2009**, *42*, 691−696.

(30) International Center for Diffraction Data (ICDD). *PDF 04-004-4243 and PDF 01-078-8777*.
(31) Yin, S.; Wang, H.; Zhao, H.; Jiang, Y.; Wang, J. The effects of Cu doping on crystalline structure and magnetic properties of $SmCo_{5-x}Cu_x$ thin films grown on Ru (0002). *J. Appl. Phys.* **2013**, *114*, 213908.
(32) Cui, W.; Ma, L.; Sepehri-Amin, H.; Takahashi, Y.; Hono, K. The influence of grain morphology and easy axis orientation on the coercivity of $Sm(Co_{0.9}Cu_{0.1})_5$ thin films. *Acta Mater.* **2016**, *107*, 49−58.
(33) Haider, S. K.; Ngo, H. M.; Kim, D.; Kang, Y. S. Enhancement of anisotropy energy of $SmCo_5$ by ceasing the coupling at 2c sites in the crystal lattice with Cu substitution. *Sci. Rep.* **2021**, *11*, 10063.
(34) Okumura, H.; Fukushima, T.; Akai, H.; Ogura, M. First-principles Calculation of Magnetocrystalline Anisotropy of $Y(Co, Fe, Ni, Cu)_5$ Based on Full-potential KKR Green's Function Method. **2022**, arXiv preprint arXiv:2204.07384,
(35) Sharma, S.; Ohmer, D.; Zintler, A.; Major, M.; Radulov, I.; Kunz, U.; Komissinskiy, P.; Xu, B.; Zhang, H.; Molina-Luna, L.; Skokov, K. P.; et al. Induction of uniaxial anisotropy by controlled phase separation in Y-Co thin films. *Phys. Rev. B* **2020**, *102*, 014435.
(36) Ohtake, M.; Nukaga, Y.; Kirino, F.; Futamoto, M. Effects of substrate temperature and Cu underlayer thickness on the formation of $SmCo_5$ (0001) epitaxial thin films. *J. Appl. Phys.* **2010**, *107*, 09A706.
(37) Kneller, E. F.; Hawig, R. The exchange-spring magnet: a new material principle for permanent magnets. *IEEE Trans. Magn.* **1991**, *27*, 3588−3560.
(38) Kallmayer, M.; Schneider, H.; Jakob, G.; Elmers, H.; Balke, B.; Cramm, S. Interface magnetization of ultrathin epitaxial Co_2FeSi (110)/Al_2O_3 films. *J. Phys. D: Appl. Phys.* **2007**, *40*, 1552−1557.
(39) Stöhr, J. Exploring the microscopic origin of magnetic anisotropies with X-ray magnetic circular dichroism (XMCD) spectroscopy. *J. Magn. Magn. Mater.* **1999**, *200*, 470−497.
(40) Sankar, S.; Rao, V.; Segal, E.; Wallace, W.; Frederick, W.; Garrett, H. Magnetocrystalline anisotropy of $SmCo_5$ and its interpretation on a crystal-field model. *Phys. Rev. B* **1975**, *11*, 435−439.
(41) Patrick, C. E.; Staunton, J. B. Temperature-dependent magnetocrystalline anisotropy of rare earth/transition metal permanent magnets from first principles: the light RCo_5 (R= Y, La-Gd) intermetallics. *Phys. Rev. Mater.* **2019**, *3*, 101401.
(42) Tils, P.; Loewenhaupt, M.; Buschow, K.; Eccleston, R. Crystal and exchange fields in $SmCo_5$ studied by inelastic neutron scattering. *J. Alloys Compd.* **1999**, *289*, 28−31.
(43) Tie-Song, Z.; Han-Min, J.; Guang-Hua, G.; Xiu-Feng, H.; Hong, C. Magnetic properties of R ions in RCo_5 compounds (R= Pr, Nd, Sm, Gd, Tb, Dy, Ho, and Er). *Phys. Rev. B* **1991**, *43*, 8593−8598.
(44) Givord, D.; Laforest, J.; Schweizer, J.; Tasset, F. Temperature dependence of the samarium magnetic form factor in $SmCo_5$. *J. Appl. Phys.* **1979**, *50*, 2008−2010.
(45) Buschow, K.; Van Diepen, A.; De Wijn, H. Crystal-field anisotropy of Sm^{3+} in $SmCo_5$. *Solid State Commun.* **1974**, *15*, 903−906.
(46) Terasawa, A.; Matsumoto, M.; Ozaki, T.; Gohda, Y. Efficient algorithm based on liechtenstein method for computing exchange coupling constants using localized basis set. *J. Phys. Soc. Jpn.* **2019**, *88*, 114706.
(47) Tripathi, S. XMCD investigation at M4,5 edges of the rare earth elements in high-performance permanent magnet. Ph.D. Thesis; Universität Stuttgart, 2018.
(48) Lamichhane, T. N.; Onyszczak, M. T.; Palasyuk, O.; Sharikadze, S.; Kim, T.-H.; Lin, Q.; Kramer, M. J.; McCallum, R.; Wysocki, A. L.; Nguyen, M. C.; Antropov, V. P.; Pandey, T.; Parker, D.; Bud'ko, S. L.; Canfield, P. C.; Palasyuk, A. Single-Crystal Permanent Magnets: Extraordinary Magnetic Behavior in the Ta-Cu- and Fe-Substituted $CeCo_5$ Systems. *Phys. Rev. Appl.* **2019**, *11*, 014052.
(49) Xie, R.; Zhang, H. Mixed valence nature of the Ce 4f state in $CeCo_5$ based on spin-polarized DFT + DMFT calculations. *Phys. Rev. B* **2022**, *106*, 224411.
(50) Matsumoto, M. Magnetism trends in doped Ce-Cu intermetallics in the vicinity of quantum criticality: Realistic Kondo lattice models based on dynamical mean-field theory. *Phys. Rev. Mater.* **2020**, *4*, 054401.
(51) Sayama, J.; Mizutani, K.; Asahi, T.; Ariake, J.; Ouchi, K.; Osaka, T. Origin of perpendicular magnetic anisotropy of $SmCo_5$ thin films with Cu underlayer. *J. Magn. Magn. Mater.* **2006**, *301*, 271−278.

https://doi.org/10.1021/acs.inorgchem.3c01768
Inorg. Chem. 2023, 62, 16354−16361